

A Growth Factor-Induced, Spatially Organizing Cytoskeletal Module Enables Rapid and Persistent Fibroblast Migration

Katrin Martin,¹ Marco Vilela,^{2,4} Noo Li Jeon,³ Gaudenz Danuser,^{2,4} and Olivier Pertz^{1,*}

¹Department of Biomedicine, University of Basel, Mattenstrasse 28, 4058 Basel, Switzerland

²Department of Cell Biology, Harvard Medical School, 240 Longwood Avenue, LHRB 301B, Boston, MA 02115, USA

³School of Mechanical and Aerospace Engineering, Seoul National University, Seoul 151-742, Republic of Korea

⁴Present address: Department of Cell Biology, UT Southwestern Medical Center, Dallas, TX 75235-5303, USA

*Correspondence: olivier.pertz@unibas.ch

<http://dx.doi.org/10.1016/j.devcel.2014.07.022>

SUMMARY

Directional migration requires robust front/back polarity. We find that fibroblasts treated with platelet-derived growth factor (PDGF) and prepolarized by plating on a fibronectin line substrate exhibit persistent migration for hours. This does not occur in the absence of PDGF or on uniformly coated fibronectin substrates. Persistent migration arises from establishment of two functional modules at cell front and back. At the front, formation of a zone containing podosome-like structures (PLS) dynamically correlates with low RhoA and myosin activity and absence of a contractile lamella. At the back, myosin contractility specifically controls tail retraction with minimal crosstalk to the front module. The PLS zone is maintained in a dynamic steady state that preserves size and position relative to the cell front, allowing for long-term coordination of front and back modules. We propose that front/back uncoupling achieved by the PLS zone is crucial for persistent migration in the absence of directional cues.

INTRODUCTION

Cells directionally migrate in response to gradients of immobilized (haptotaxis) or diffusible (chemotaxis) cues (Parsons et al., 2010). Extracellular matrix (ECM) rigidity or dimensionality can also modulate this process (Petrie et al., 2009). Combinations of these cues will affect parameters such as cell speed, shape, and directionality, producing a continuum of cell migration modalities (Friedl and Wolf, 2010). Whereas the diversity of cell migration modalities is well accepted, they have been described in a wide variety of different model systems, making fair comparisons difficult. Accordingly, our understanding as to how the dynamics of the migration machinery is modulated to establish particular migration modes is still limited.

Fibroblasts are large mesenchymal cells that are mostly involved in tissue repair. Due to their well-defined cytoskeleton organization, they have been a popular model system to study

actin and adhesion dynamics during cell migration. At the front, two cytoskeletal modules are coupled with integrin-based adhesion structures to allow cell propulsion (Ponti et al., 2004). The lamellipodium uses Arp2/3-mediated assembly of an actin dendritic meshwork to propel the leading edge forward (Pollard and Borisy, 2003). Nascent adhesions are formed and can mature into focal complexes. Behind the lamellipodium, the lamella consists of bundled actin and nonmuscle myosin II filaments that provide a contractile network for traction. Here, focal complexes mature into stress fiber-linked, elongated focal adhesions (Parsons et al., 2010). Linkage of front and back focal adhesions through stress fibers, coupled with propulsion of the leading edge, moves the cell forward, and leads to disassembly of back focal adhesions and tail retraction. Podosomes are an additional type of adhesions that consist of a central actin core associated with integrins and other proteins (Murphy and Courtneidge, 2011). They are observed in a wide variety of immune and cancer cells (Calle et al., 2006) and are found in Src-transformed fibroblasts (Oikawa et al., 2008). Podosome substrate interaction leads to local ECM degradation and invasion.

One important limitation of fibroblasts is their moderate capability to robustly polarize during random migration on uniform ECM fields (haptokinesis) or in response to global growth factor stimulation (chemokinesis). Thus, on planar ECM substrates, unrestricted membrane protrusion leads fibroblasts to adopt a wide variety of cellular shapes with various degrees of polarization. Although this is sufficient to study the fine dynamics of membrane protrusion and tail retraction, it precludes the analysis of how both processes are coordinated to produce net movement. In vivo, fibroblasts interact with ECM structures of specific geometries that influence cell polarization (Kim et al., 2012). Hence, fibroblasts migrating on micrometric ECM line patterns exhibit increased migration speed and directionality (Doyle et al., 2009). Mimicking the anisotropic ECM organization observed in vivo therefore provides an opportunity to induce robust fibroblast polarization.

Rho family GTPases are key regulators of the spatio-temporal organization of actin and adhesion dynamics during cell migration. While initial models suggested that Rac1 and Cdc42 operate at the front to regulate membrane protrusion, and RhoA functions at the back to control tail retraction (Burridge and Wennerberg, 2004), recent studies using fluorescence

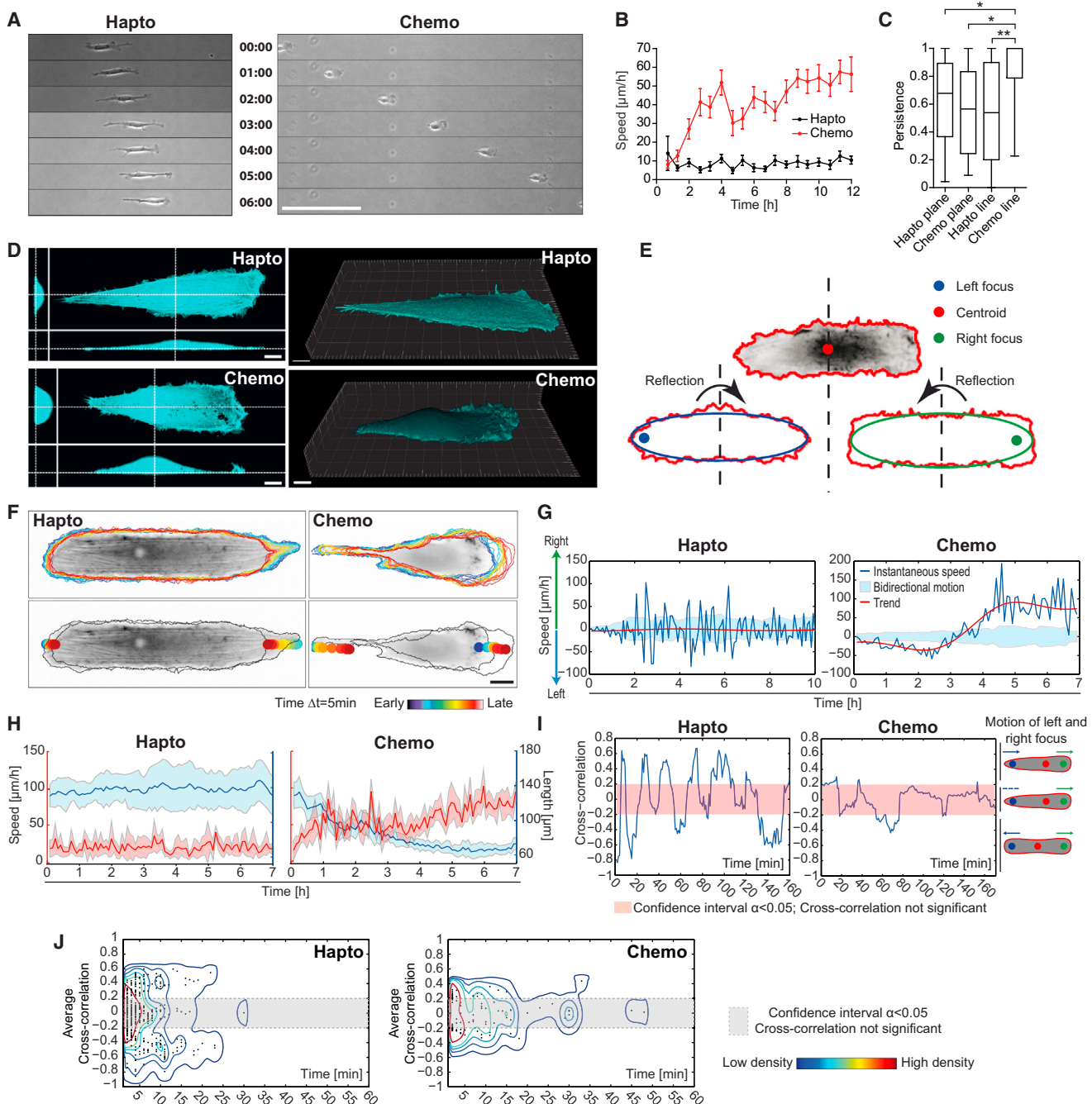


Figure 1. Characterization of Hapto and Chemo Cell Migration on the Line Substrate

(A) Representative phase contrast time series of hapto and chemo cell migration on line substrates.

(B) Time course of instantaneous speed. Speed \pm SEM is shown ($n \geq 20$ cells).

(C) Cell migration persistence. Boxplots of net over total travel distance during steady state migration (6 hr until 12 hr post-PDGF stimulation); median, interquartile (box) and data (whiskers) ranges are shown. * $p < 0.005$, ** $p < 0.001$; ($n \geq 19$ cells; Dunn's multiple comparison test).

(D) Confocal imaging of phalloidin stained hapto and chemo cells. Left: xy, xz, and yz cross-sections. Right: 3D reconstructions of fibroblasts.

(E) Strategy for identification of centroid and left and right foci. Cell centroid is first identified using the segmented outline of the cell. Ellipse fitting to reflected (left and right) halves defines left and right foci, representing independent cell motions at both cell edges.

(F) Examples of cell segmentation of hapto and chemo cells. Cell outlines (upper); and movements of left and right foci (lower) are color-coded according to time. Cells were plated in absence or presence of 40 ng/ml PDGF, and time-lapse analysis was started 1–2 hr postplating using a 20 \times air objective.

(G) Representative time courses of centroid velocities for hapto and chemo cells (dark blue line). Red line, low variation trend speed. Light blue bands indicate 95% confidence intervals of bidirectional motion. In phases in which the trend speed is outside the band, the cell transiently establishes directed motion. See the Experimental Procedures for complete description of time course decomposition in high and low variation components.

(legend continued on next page)

resonance energy transfer (FRET)-based biosensors have indicated a higher level of signaling complexity (Machacek et al., 2009; Pertz et al., 2006). Most importantly, RhoA signaling is also active at the cell front, where during fibroblast haptokinesis, two distinct activities are observed: Adjacent to the leading edge, a focused region of RhoA activity is coupled to the initiation of edge protrusion (Machacek et al., 2009). This is followed by a broader gradient of RhoA activity reaching 10–15 μm into the lamella (Pertz et al., 2006). Rac1 and Cdc42 are also activated at the front, however, with a delay relative to protrusion onset (Machacek et al., 2009). This organization is fundamentally altered when fibroblasts are acutely stimulated with platelet-derived growth factor (PDGF), which leads to heightened cell edge protrusion and membrane ruffling. Here, RhoA activity is displaced from the leading edge (Pertz et al., 2006), and supposedly replaced by heightened Rac1 and Cdc42 activity. Hence, dependent on the cue, different Rho GTPase signaling programs are activated to induce distinct modes of cell migration.

In this paper, we dissect the mechanisms underlying the differences of fibroblast haptokinesis and PDGF-induced chemokinesis on micropatterned fibronectin (FN) line substrates. We find that PDGF-treated fibroblasts exhibit persistent cell migration for hours. This correlates with the formation of a zone containing podosome-like structures (PLSs) directly behind the lamellipodium that exhibits constant size and position. The PLS zone dynamically correlates with low RhoA and myosin activity, and precludes the formation of a lamella. Instead, myosin activity is concentrated behind the PLS zone to promote tail retraction. Thus, the PLS zone spatially organizes the formation of two distinct modules, one for membrane protrusion and one for tail retraction, enabling persistent migration.

RESULTS

PDGF Induces Persistent Migration of Prepolarized Fibroblasts

To compare haptokinetic (hapto) and PDGF-induced chemokinetic (chemo) cell migration modes, we used REF52 rat embryonic fibroblasts, a classic model system to study actin and adhesion dynamics (Zamir et al., 1999). Throughout this work, we used the following conditions: serum-starved REF52 fibroblasts were plated on 10 μg/ml FN-coated coverslips in absence (hapto) or presence of 40 ng/ml PDGF (chemo). On uniformly coated plane substrates, both hapto and chemo fibroblasts migrate randomly with an instantaneous speed of ~10 μm/hr (Figures S1A–S1C available online). Although not significant at the population level, a fraction of chemo cells displayed increased directional persistence (Figure S1B). To normalize cell shape and mimic the anisotropic nature of the ECM observed *in vivo*, we used plasma etching to construct 20 μm wide 10 μg/ml FN lines separated by the nonadhesive compound

poly-L-Lysine-polyethylene glycol (PLL-PEG; Figure S1D). This allowed FN coating at a density identical to the coat on the plane substrate (Figures S1E and S1F). Hapto cells on line substrate adopted an elongated morphology and exhibited similar instantaneous speed and persistence as on plane substrates (Figures 1A, 1B, and S1C). In contrast, chemo cells gradually sped up on line substrates, reaching a 5-fold increase in instantaneous speed within hours after PDGF stimulation and acquired a steady state in which they stably migrated in one direction (Figures 1A–1C). Both steady state speed and persistence scaled inversely with the FN coating density (Figures S1G and S1H). The differences between hapto and chemo cells in terms of migration properties were accompanied by acquisition of distinct cell morphologies. Hapto cells were elongated and flat, whereas chemo cells exhibited a strongly ruffled leading edge, a thick cell body, and an obvious trailing edge (Figure 1D). Together, these results show that PDGF stimulation of fibroblasts that are prepolarized on a FN line substrate induces rapid, persistent, and unidirectional cell migration.

Polarization of Chemo Cells Involves a Morphological Transition with Uncoupling of Front and Back Motions

The cell shape normalization on the line substrate enabled us to unambiguously define cell front and back and thus to study their coordination. For that purpose, we acquired time-lapse sequences of fibroblasts stably expressing the F-actin marker Lifeact-green fluorescent protein (GFP; Riedl et al., 2008). To quantify cell migration morphodynamics at relevant time scales, we designed an automated segmentation algorithm to evaluate the dynamics of front, centroid, and back parts (Figures 1E and 1F; Movie S1). Hapto cells exhibited alternating left and right motions, indicating the existence of transient polarization episodes that impede persistent cell migration (Figure 1G). In contrast, a few hours after PDGF stimulation, chemo cells acquired a stably polarized state of persistent migration (Figure 1G). This correlated with increased speed and decreased cell length, whereas these parameters remained constant throughout time in hapto cells (Figure 1H).

We then evaluated the coordination between cell front and back movements by performing time-dependent cross-correlation analysis of velocity fluctuations (Experimental Procedures and Figure S1I). Hapto cells displayed transient episodes of strongly positive and strongly negative cross-correlations (Figures 1I and 1J), where front and back move coordinately in identical or opposite directions. This indicates that at least during episodes of comovement, front and back motions are coupled. In contrast, chemo cells did not exhibit robust positive or negative cross-correlations (Figures 1I and 1J), suggesting that front and back movements are uncoupled. Thus, establishment of the steady state of persistent migration in chemo cells occurs on time scales of hours and involves a morphological transition

(H) Average time courses of cell speeds (red) and lengths (blue), n = 21 chemo cells, n = 16 hapto cells. Light blue and red intervals represent the 95% confidence interval around the mean value. Note that different cell trajectories were aligned in time to faithfully represent the transition to a polarized phenotype.

(I and J) Motion coordination between left and right foci as quantified by cross-correlation. See experimental procedures for the time-dependent cross-correlation algorithm. (I) Single cell, foci motion cross-correlation traces. Cartoons indicate possible states of focus motion yielding positive, null, and negative cross-correlation. (J) 2D distribution of the average cross-correlation (y axis); duration of all instances of uniform qualitative behavior (x axis). Data from n = 13 cells (hapto), n = 10 cells (chemo).

Scale bars represent (A) 100 μm and (D and F) 10 μm.

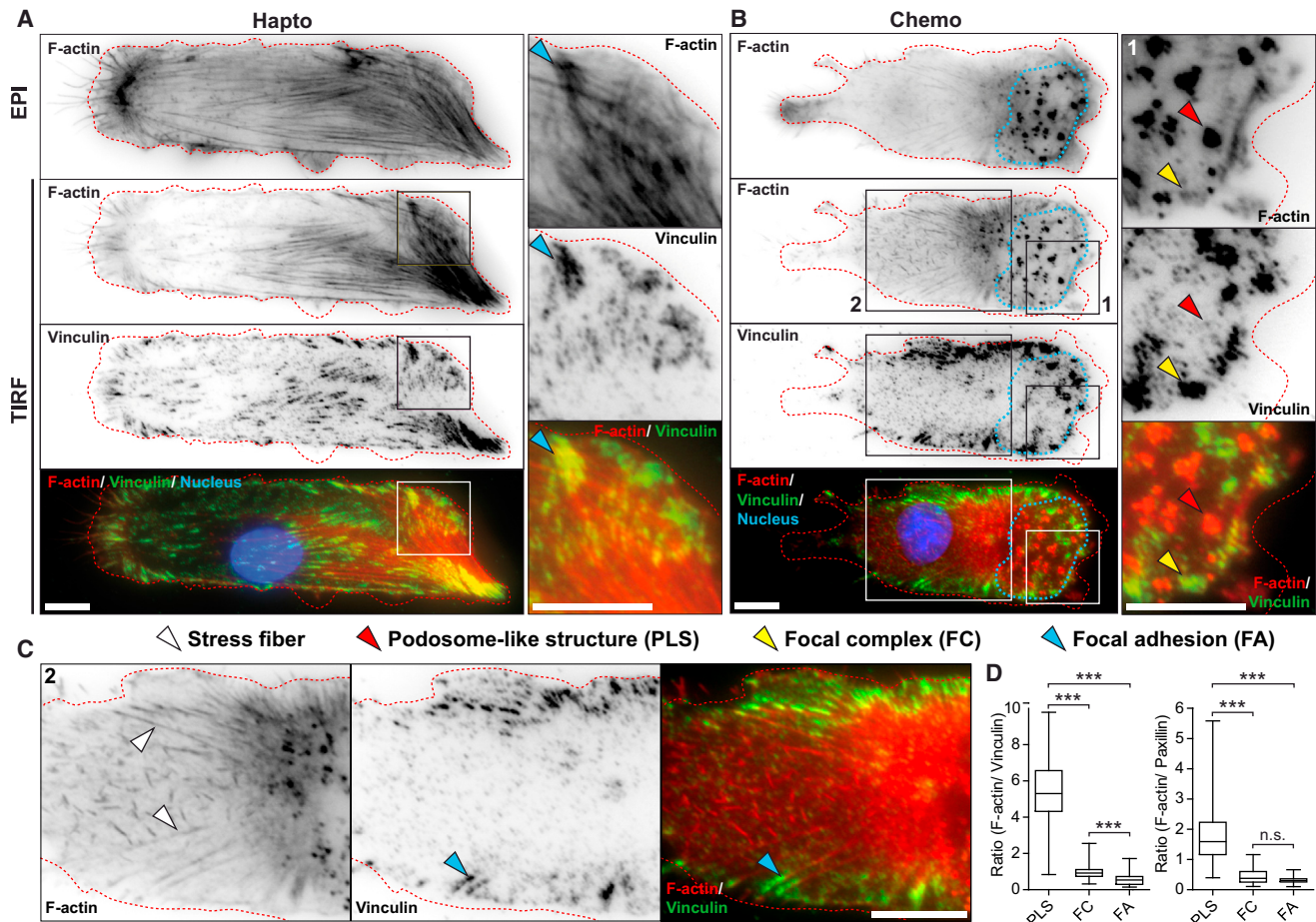


Figure 2. Actin and Adhesion Structures in Hapto and Chemo Cells

Micrographs are shown in inverted black and white contrast (ibw) or as color composites.

(A and B) Representative F-actin and vinculin stainings in hapto (A) and chemo (B) cells. Cells were fixed 6 hr postplating, stained with phalloidin-alexa555 and anti-vinculin antibody, and imaged using EPI or TIRF microscopy. A DAPI nuclear stain was also included. Magnified insets of leading edge are shown. Blue outline delineates the PLS zone.

(C) Magnified inset of the back region of the chemo cell in (B). White arrowhead denotes rear contractile F-actin network, blue arrowhead points to focal adhesions.

(D) Quantification of F-actin/vinculin or paxillin fluorescence ratios of different adhesion structures. Mean fluorescence intensity of F-actin and adhesion component were ratioed using threshold masks in the same cell. Ratio F-actin/vinculin: 5 cells, n = 98 PLSs, 112 focal complexes, 82 focal adhesions; ratio F-actin/paxillin: 5 cells, n = 162 PLSs, 187 focal complexes, 77 focal adhesions. Boxplots with median, interquartile (box), and data (whiskers) ranges are shown.

***p < 0.001 (Dunn's multiple comparison test).

Scale bars represent 10 μm (A–C).

that correlates with increased velocity. Furthermore, the polarized steady state of chemo cells correlates with uncoupling of front and back motions.

Chemo Cells Display Podosome-like Structures at the Leading Edge

The distinct cell morphologies suggest that hapto and chemo cell migration modes are mediated by different cytoskeletal and adhesion dynamics. To test this we used high-resolution immunostaining using epifluorescence (EPI) and total internal reflection fluorescence (TIRF) microscopy. Transiently polarized hapto cells displayed asymmetric distributions of front-enriched stress fibers and focal adhesions (Figure 2A). A network of transverse stress fibers connected leading edge and lateral focal

adhesions, whereas a lower amount of focal adhesions was observed at the trailing edge. Focal adhesions at front and back were connected by lateral stress fibers. In contrast, stably polarized chemo cells overall had fewer stress fibers (Figure 2B). A large region at the leading edge displayed dotted F-actin-rich/vinculin-low PLSs (Figure 2B; red arrowheads, PLS; dotted blue line, PLS zone). Although PLSs did not display the bona fide F-actin core surrounded by a ring containing adhesion structures as observed in podosomes (Albiges-Rizo et al., 2009), they displayed proteolytic activity on a gelatin line substrate (Figure S2A) and were enriched in cortactin (Figure S2B). Within the PLS zone, we also observed F-actin-low/vinculin-rich structures not connected to stress fibers (Figure 2B, yellow arrowheads) that were reminiscent of focal complexes. Focal adhesions were

absent within the PLS zone. Immediately behind the PLS zone, TIRF microscopy revealed a network of ventrally localized transverse actin fibers (Figure 2C, white arrowhead). This network was not connected to any adhesion structure in the cell center, but associated with elongated focal adhesions confined to the lateral edges and the back of the cell (Figure 2C, blue arrowheads). To clearly distinguish these different adhesion structures, the relative enrichment between F-actin and vinculin or paxillin fluorescence signals in PLSs, focal complexes and focal adhesions in chemo cells is quantitated in Figure 2D. Overall, such organization with a PLS zone was observed in 70% of chemo cells on lines (Figure S2C). These results indicate the existence of different actin and adhesion structures in haptotaxis and chemo cells.

Chemo Cells Lack a Contractile Lamella

We subsequently monitored actin dynamics in both cell migration modes using the F-actin marker Lifeact-GFP (Movie S2). In haptotaxis cells, the lamellipodium remained continuously attached to the substrate, leading to a highly adherent mode of membrane protrusion (Figure 3A, lower panels). Formation of actin arcs (Hotulainen and Lappalainen, 2006) indicated robust actin retrograde flow in the lamella as well as on the lateral sides (Figure 3A, kymographs 1 and 2, quantitated in Figure 3C). In marked contrast, in chemo cells, the lamellipodium was characterized by rapid bursts of filopodial and membrane protrusions that escaped the TIRF illumination field. This indicates a low adhesive protrusion mode because these structures extend in Z before contacting the substrate (Figure 3B, lower panels). Directly behind the lamellipodium, the lamella was replaced by the PLS zone (Figure 3B, kymograph 1) with absence of contractile, rearward-flowing actin arcs. This suggests that actin retrograde flow is confined to the lamellipodium but mostly absent from the PLS zone. Live cell imaging also revealed that PLSs specifically originate in the lamellipodium that extends on the permissive FN substrate, remain immobile with respect to the substrate (Figure 3B, kymograph 1, red arrowheads), and display a lifetime of about 10 min (Figure 3G). Accordingly, the PLS zone remained constant in size throughout cell migration (Figure 3B, dotted white lines in kymograph 1). Robust actin retrograde flow persisted on the sides as observed by inward flow of lateral arcs (Figure 3B, kymograph 2, quantitated in Figure 3C).

We then observed adhesion dynamics (Figures 3D–3G; Movie S3) and noticed that chemo cell polarization and formation of the PLS zone was highly sensitive to exogenous expression of GFP-tagged cytoskeletal or adhesion proteins, even when stably expressed at low level. This required two-color imaging experiments, in which we first produced stable cell lines using a lentiviral system for low expression of GFP-tagged proteins, then used an adenovirus system to coexpress Lifeact-mCherry for identification of polarized chemo cells. We tested a number of different constructs, and found that VASP-GFP was the adhesion marker that was least perturbing. In haptotaxis cells, focal complexes immediately converted to focal adhesions, most likely through interaction with the contractile lamella (Parsons et al., 2010; Figures 3D and 3E; Movie S3, haptotaxis, blue arrowheads). These focal adhesions displayed typical centripetal sliding behavior (Figure 3F) with a lifetime of approximately 30 min (Figure 3G). Chemo cells displayed both PLSs (F-actin-high/

VASP-low, red arrowheads) and focal complexes (F-actin-low/VASP-high, yellow arrowheads) at the leading edge (Figures 3D and 3E). Nonmotile PLSs grew and shrunk in lateral extension-decay cycles (Figure 3F, red arrowheads). Within the PLS zone, VASP-GFP revealed that focal complexes also remained immobile relative to the substrate (Figure 3F, yellow arrowheads) and almost never matured into focal adhesions. Thus, they display identical lifetimes as PLSs (Figure 3G). Elongated focal adhesions were only observed on the lateral edges and at the back of the cells, and exhibited sliding motions (Figure 3F, chemo, blue arrowheads), most likely through pulling by the SF array emanating from the cell center (Movie S3). Together, these results show that the contractile lamella observed in haptotaxis cells is replaced by the PLS zone in chemo cells. Absence of a contractile lamella correlates with loss of focal complex-focal adhesions maturation within the PLS zone, leading to their turnover, and restricting focal adhesions to the back and lateral sides of the cell.

Establishment of Steady-State, Persistent Chemo Cell Migration Correlates with Appearance of the PLS Zone

The steady state of persistent chemo cell migration is acquired hours after PDGF stimulation and is then characterized by a dynamic PLS zone at the leading edge. To explore how this polarized steady state is established, we performed high-resolution time-lapse imaging of F-actin dynamics during the first 7 hr after PDGF stimulation. On the line substrate, haptotaxis cells continuously exhibited robust, symmetric stress fibers that correlate with left-right motions impeding long-term polarization (Movie S4). PDGF stimulation led to a stereotypical series of morphological states that culminated in the steady state of polarized cell migration (Figures 4A and 4B; Movie S4). Immediately after PDGF stimulation, chemo cells on the line substrate exhibited intense ruffling, which correlated with decreased amounts of stress fibers. Two to three hours later, a robust PLS zone suddenly appeared at one cell edge, but the cell body was still adherent. Tens of minutes later, the presence of a robust PLS zone and rounding up of the cell body then correlated with persistent, rapid cell migration. As already observed on smaller time scales, the PLS zone remained at the leading edge and displayed constant length (Figure 4C). These results indicate that acquisition of the polarized steady state of persistent migration coincides with appearance of the PLS zone.

The PLS Zone also Occurs in Chemo Cells on Plane Substrates

On the plane substrate, haptotaxis cells also continuously exhibited prominent actin arcs that retrogradely flowed inward throughout the periphery (Movie S4). This correlated with robust focal adhesion formation; however, with shorter lifetimes than on the line substrate (Figures S3A–S3C and S3G). In chemo cells, PDGF stimulation initially led to intense ruffling that then dampened (Movie S4). This was followed by appearance of multiple PLS zones that exhibit scanning motions at the cell periphery (Figure 4D) and were intermixed with regions of actin retrograde flow. These PLS zones were unstable and only persisted on time scales of tens of minutes (Figure 4D; Movie S4). High-resolution analysis using TIRF indicated that PLSs were nonmotile with respect to the substrate (Figures S3D–S3F) and displayed

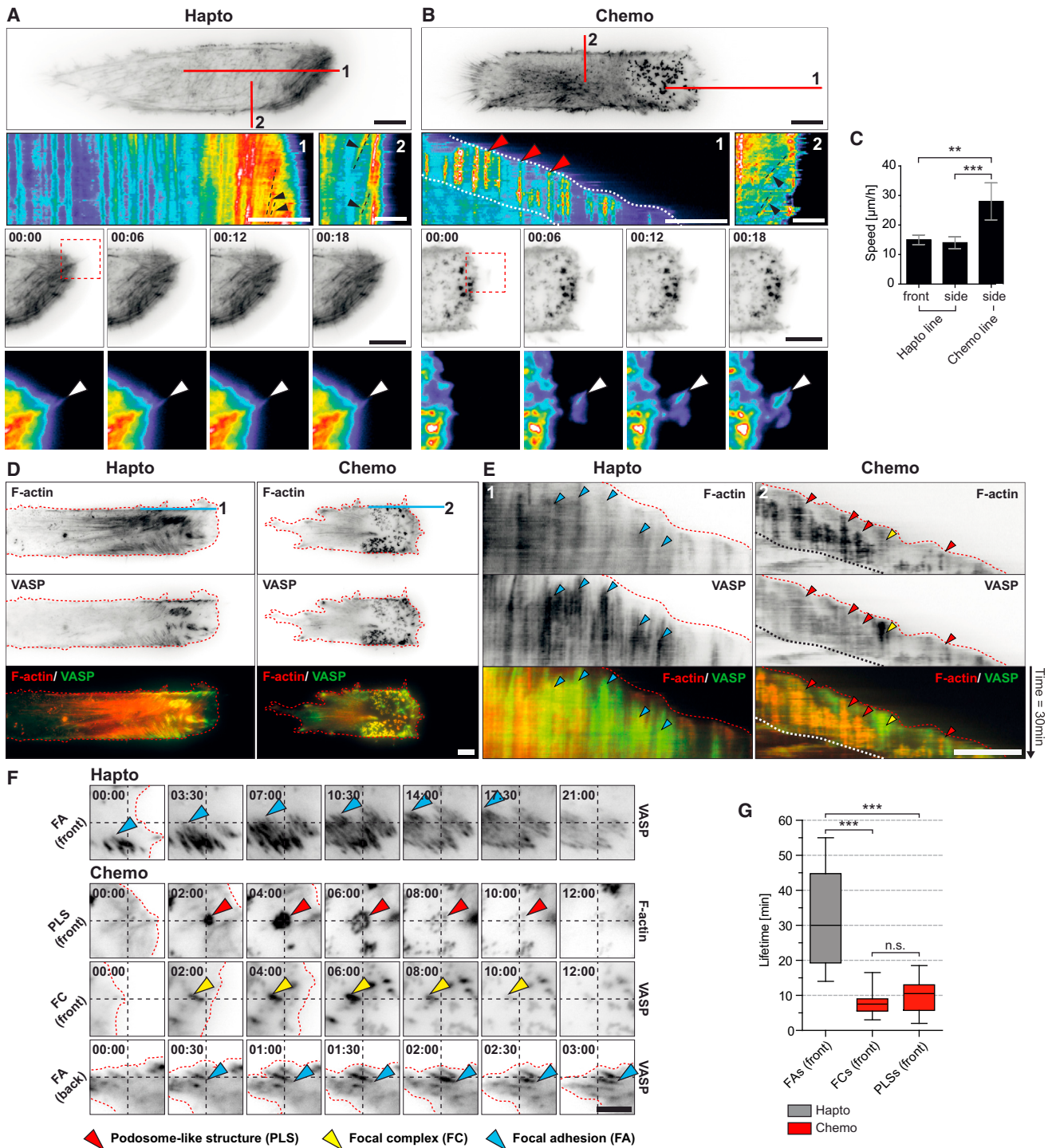


Figure 3. Actin and Adhesion Dynamics in Hapto and Chemo Cells

(A and B) Representative micrographs, time series (min:s), and inset zooms of Lifeact-GFP signals using TIRF in hapto (A) and chemo (B) cells. Kymographs are used to analyze actin dynamics at the leading (1) and lateral edges (2). Black arrowheads indicate actin arcs used to measure actin retrograde flow velocity. Lower: white arrowheads indicate membrane protrusions. (B) Vertical streaks in the kymograph (indicated by red arrowheads) show that PLSs originate at the leading edge, are nonmotile with respect to the substrate, and display constant lifetimes. White dotted lines delineate PLS zone.

(C) Quantification of actin retrograde flow velocity by kymograph analysis. Hapto: n = 9 cells, chemo: n = 5 cells, error bars indicate \pm SEM, **p < 0.001, ***p < 0.0001; Dunn's multiple comparison test.

(D) Representative micrographs of VASP-GFP and Lifeact-mCherry signals in hapto and chemo cells.

(E) Kymographs of lines drawn in (D). Blue arrowheads point to focal adhesions, yellow arrowheads point to focal complexes, red arrowheads point to PLSs.

(legend continued on next page)

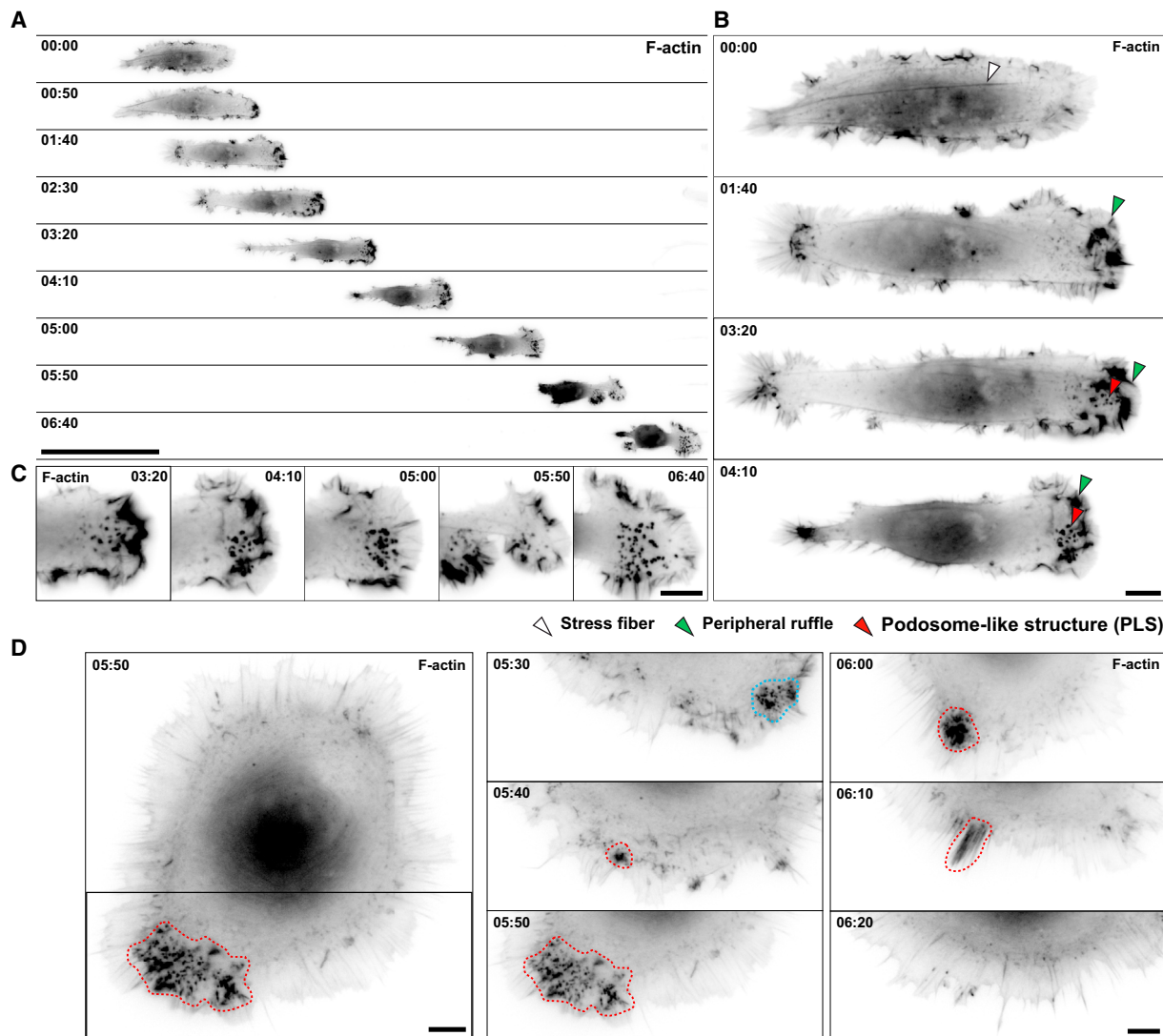


Figure 4. Kinetics of Establishment of the Chemo Cell Polarized Migration Steady State

Cells were stimulated with 40 ng/ml PDGF and immediately time-lapsed for F-actin dynamics (Lifeact-GFP) for 7 hr using a 40× air objective. Multiple fields of view were stitched to depict the whole polarization process. Time is in hr:min.

(A) Low-resolution view of a time series of a chemo cell.

(B) Representative high-resolution images of different polarization stages. 00:00, contractile stage; 01:40, ruffling; 3:20, appearance of PLS zone with cell body adherent; 04:10, PLS zone and loosely adherent cell body.

(C) High-magnification views of the PLS zone after acquisition of the steady state of polarized cell migration.

(D) Chemo cell on the plane substrate. Left: Fluorescent micrograph of a chemo cell. Right: time series depicting PLS zone dynamics. Different PLS zones are indicated by dotted lines. Dotted blue (05:30) and red lines (06:00–06:20) highlight different temporally defined PLS zones.

Scale bars represent (A) 100 μm; (B–D) 10 μm.

shorter lifetimes than on the line substrate (on the order of 2–3 min, Figure S3G). The apparent motile behavior of PLS zones, observed at a global scale, resulted from cycles of single PLS appearance/disappearance. Focal complexes present within

the PLS zone did not mature to focal adhesions and displayed identical lifetimes than PLSs (Figure S3D–S3G). These cytoskeletal dynamics correlated with a higher level of polarization of chemo versus haptotactic cells, characterized by a lower aspect ratio

(F) Representative time series of front and back adhesions and podosomes. Dashed crosshair provides reference for virtual inspection of motile behaviors of the adhesions. Arrowheads are color-coded as in (E).

(G) Boxplots of lifetimes of leading edge adhesions and PLSs; median, interquartile (box), and data (whiskers) ranges are shown. n ≥ 5 cells each, ≥ 20 adhesions per cell, 87 PLSs, ***p < 0.0001; Dunn's multiple comparison test.

Scale bars represent (A, B, D, and E) 10 μm and (F) 5 μm.

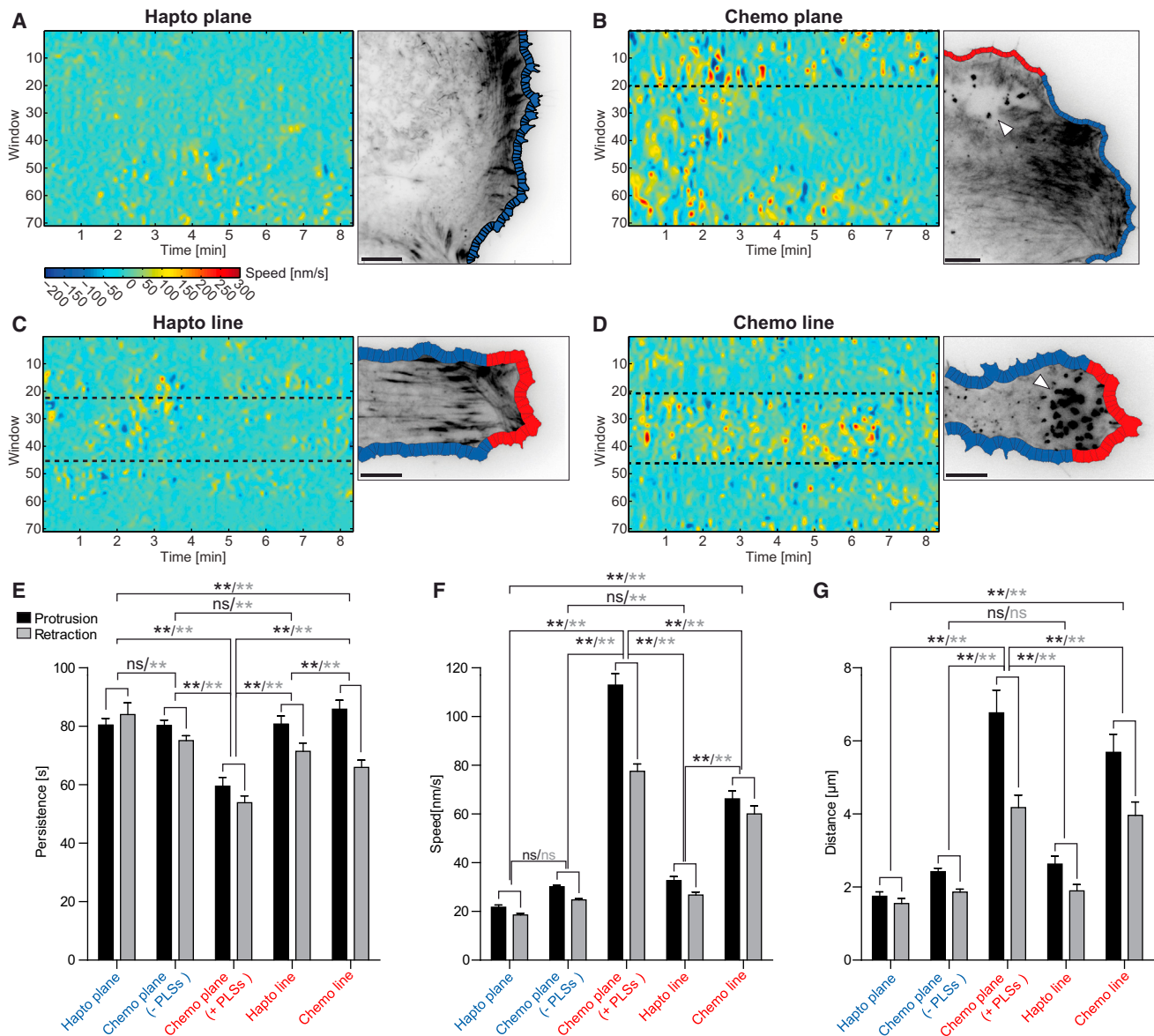


Figure 5. Dynamics of Leading Edge in Hapto and Chemo Cells

Micrographs are shown in ibw contrast.

(A–D) Space-time maps of edge velocities and representative cell edges indicating segments used for the analysis. Edge velocities are color-coded according to scale with protrusions displayed in warm and retractions displayed in cold colors. (C and D) Dotted lines indicate edge dynamics on the permissive substrate. (B) Dotted lines indicate edge segments containing PLSs.

(E–G) Quantification of different metrics characterizing membrane protrusion dynamics. Average persistence times (E), speed (F), and traveled distance (G), n ≥ 5 cells each, ±SEM, **p < 0.001; Dunn's multiple comparison test.

Scale bars represent 10 μm (A–D).

(hapto: 0.27 ± 0.06 , n = 13 cells; chemo: 0.17 ± 0.04 , n = 16 cells, ***p < 0.0001). These results show that on the plane substrate, transient establishment of PLS zones associates with localized loss of contractile structures such as actin arcs and focal adhesions and only correlates with mild polarization. On the line substrate, the PLS zone is geometrically confined and correlates with loss of contractile networks and lamella formation at one cell edge, which is associated with robust polarization.

Hapto and Chemo Cells Display Different Leading Edge Dynamics

We next investigated the dynamics of the leading edge in high-resolution time-lapse sequences sampled at 5 s per frame. We quantified the dynamics of edge protrusion and retraction as previously described (Machacek and Danuser, 2006). Protrusion velocity maps were generated for hapto and chemo cells both on plane and line substrates (Figures 5A–5D) and statistically evaluated (Figures 5E–5G). Hapto cells on the plane substrate

displayed poorly protrusive edges, with low velocities and no obvious persistence (Figure 5A). Spatial clustering of locally measured edge velocities revealed two populations of edge dynamics in chemo cells on the plane substrate. Remarkably, they specifically associated either with the PLS zone (red edge) or contractile networks (blue edge; Figure 5B). Whereas the speed of the PLS-associated edge was enhanced, it displayed low protrusive persistence, but still promoted efficient net protrusion. The contractile edge displayed similar properties as those observed in haptotaxis cells (which had only one type of protrusion dynamics). On the line substrate, haptotaxis cells displayed a slight enhancement of edge velocity and protrusion persistence (Figure 5C). Chemo cells displayed enhancement of both protrusion persistence and speed, resulting in a higher net protrusive activity (Figure 5D, red edges). These results indicate that the noncontractile PLS zone associates with a highly protrusive leading edge, prominently on line substrates, but present also locally on plane substrates.

Chemo Cells Assemble a Myosin Cluster Directly behind the PLS Zone for Trailing Edge Retraction

The absence of a contractile lamella in chemo cells raised the question of their migration dependence on nonmuscle myosin II (myosin)-based contractility. To address this, we evaluated the subcellular localization and dynamics of myosin light chain 2a (MLC2a) and of its active Ser19 phosphostate (pMLC). In haptotaxis cells, pMLC and MLC2a prominently decorated stress fibers (Figures 6A and S4A, Haptotaxis), whereas pMLC additionally labeled the lamella (Figure 6A, Haptotaxis, red arrowhead). Identical patterns were observed on plane substrates (Figure S4B, Haptotaxis). In contrast, both pMLC and MLC2a were absent from the chemo cell front and localized to a cortical cluster positioned behind the PLS zone, that coincided with the transverse stress fiber array that connects to focal adhesions at the lateral sides and back of the cell (Figures 6A and S4A, Chemo, red arrowhead). Outside the cluster, faint MLC2a staining remained present on these stress fibers. On the plane substrate, chemo cells displayed mixed pMLC patterns: whereas the PLS zone was devoid of any pMLC signal, pMLC localized both as a cluster adjacent to the PLS zone, as well as to peripheral contractile arrays (Figure S4B, Chemo). Live imaging of MLC2a-GFP and Lifeact-mCherry dynamics revealed constant association between MLC2a and stress fibers in haptotaxis cells (Figures 6B and 6C, Haptotaxis; Movie S5). In chemo cells, apposed but mutually exclusive PLS and MLC2a zones of constant size occurred throughout cell migration (Figures 6B and 6C, Chemo; Movie S5).

To test the functional significance of myosin-based contractility, we used blebbistatin (Straight et al., 2003) to acutely inhibit myosin ATPase activity (Figure S4C, Haptotaxis). Whole cell kymograph analysis showed that haptotaxis cells lost their transient polarized state by extending uncontrolled membrane protrusions in all directions (Figure 6D; Movie S6), which correlated with a decrease in front/back coordination (Figure 6F, Haptotaxis). Chemo cells were specifically impaired in tail retraction, but displayed almost unaffected leading edge membrane protrusion (Figure 6E). This correlated with loss of the pMLC cluster in chemo cells without affecting PLSs (Figure S4C, Chemo). On a time scale of 12 hr, loss of myosin-based contractility decreased chemo cell migration persistence without affecting (Fig-

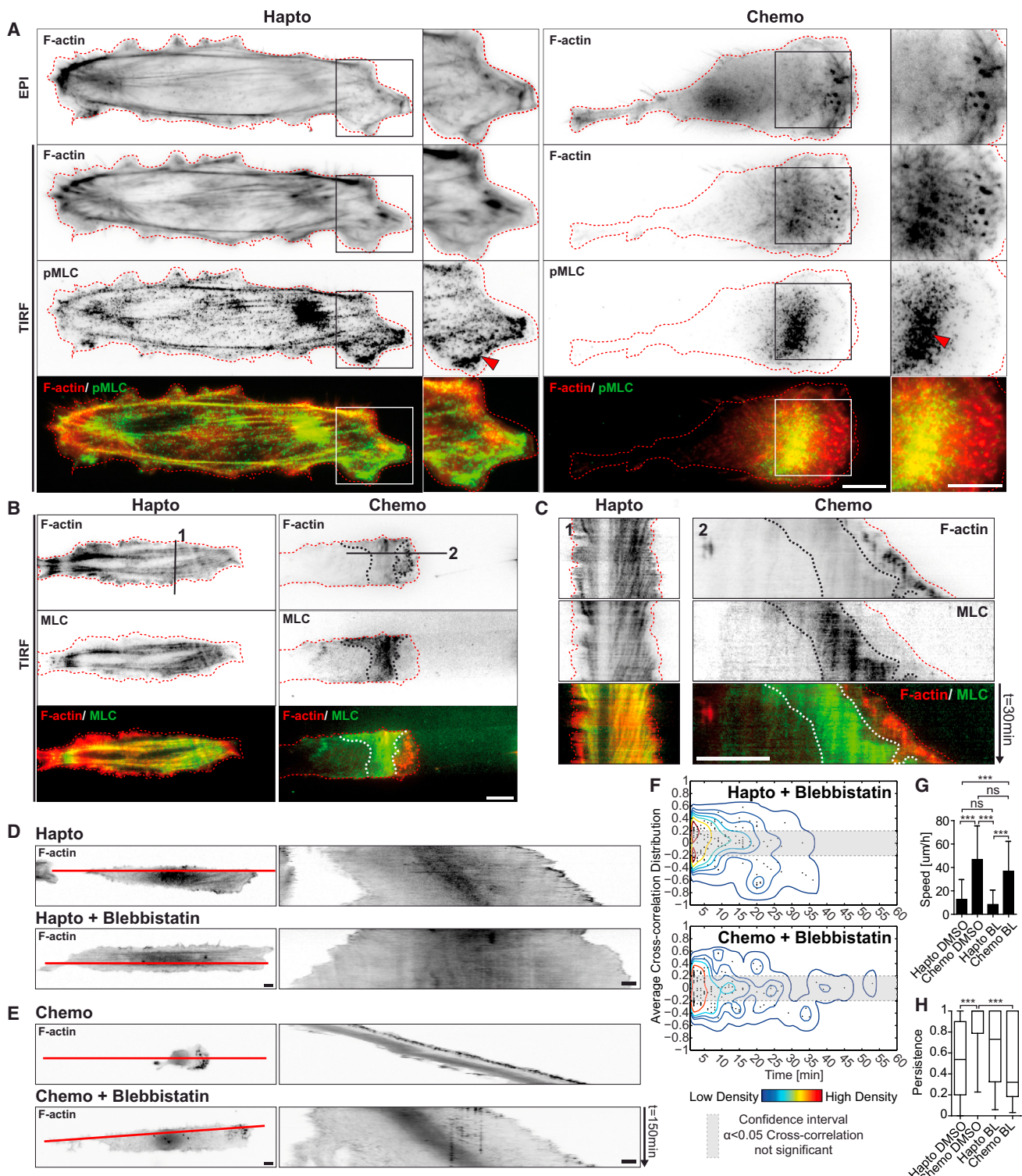
ures 6G and 6H). This occurred because of extreme stretching of chemo cells that ultimately led to their turning. Blebbistatin-treated haptotaxis cells displayed no decrease in speed (Figures 6G and 6H). These results show that myosin activity occurs in the lamella and stress fiber network of haptotaxis cells, and its inhibition deregulates overall edge protrusion and migration. In contrast, in chemo cells, PLSs establish functionally distinct cytoskeleton structures, one without (front), and one with (back) myosin-driven contractility. Myosin inhibition then only affects tail retraction whereas the lamellipodial machinery in front of the PLS remains intact.

Inhibition of the PLS Zone Rescues a Contractile Lamella in Chemo Cells

The lack of myosin activity within the PLS zone of chemo cells prompted us to explore if it directly inhibited contractile function. To this end, we tested a panel of drugs and identified the Arp2/3 inhibitor CK666 (Nolen et al., 2009) and the Src inhibitor PP2 (Oikawa et al., 2008) as appropriate compounds to acutely remove PLSs. Indeed, CK666 does not only affect PLSs, but also Arp2/3 pools involved in lamellipodial protrusion. Consistently, in both haptotaxis and chemo cells, treatment with 200 μ M CK666 led to the appearance of spiky protrusions (Figure 7A; Movie S6) as previously described (Wu et al., 2012). This however did not markedly inhibit cell migration for 1 hr. Adhesion dynamics in haptotaxis cells were only minimally affected (Figure 7A, blue arrowheads; Movie S7), as well as pMLC signals (Figure 7B, Haptotaxis). In chemo cells, CK666 treatment led to rapid removal of PLSs, which was concomitant with immediate appearance of stress fibers and focal adhesions at the leading edge (Figure 7A, blue arrowheads; Movie S7). pMLC signals relocalized from the back of the PLS zone to the leading edge, in a pattern reminiscent of the lamella of haptotaxis cells (Figure 7B). CK666 treatment did however not revert chemo cells to a contractile state as intense as in haptotaxis cells. At a global level, CK666 only minimally affected haptotaxis cell morphodynamics, with temporal cross-correlation analysis still indicating the presence of front/back coordination (Figures 7C and 7E; Movie S6). Chemo cells, however, only remained polarized for approximately 1 hr after CK666 treatment, and then lost persistent migration (Figure 7D; Movie S6). During this first 1-hr polarized cell migration episode, strong front/back motion correlations were observed, indicating that abrogation of the PLS led to linkage of cell front and back (Figure 7F). To strengthen these results, we inhibited Src using 12.5 μ M PP2, which led to immediate removal of PLSs in chemo cells. Although this only marginally affected focal adhesion dynamics and pMLC signals in haptotaxis cells (Figures S5A and S5C), immediate maturation of focal complexes to focal adhesions and rescue of leading edge pMLC signals occurred in chemo cells upon PLS disruption in 3–4 min (Figures S5B and S5D). At longer time scales, Src inhibition also affected tail retraction, precluding the analysis of global cell migration properties. Together, these results indicate that the PLS zone inhibits myosin contractility responsible for lamella formation, which is required for front/back uncoupling.

PLSs Dynamically Correlate with Low RhoA Activity in Chemo Cells

The absence of contractility—absence of actin arcs, focal complex-focal adhesion maturation and pMLC—within the PLS

**Figure 6. Characterization of the Back Myosin Module**

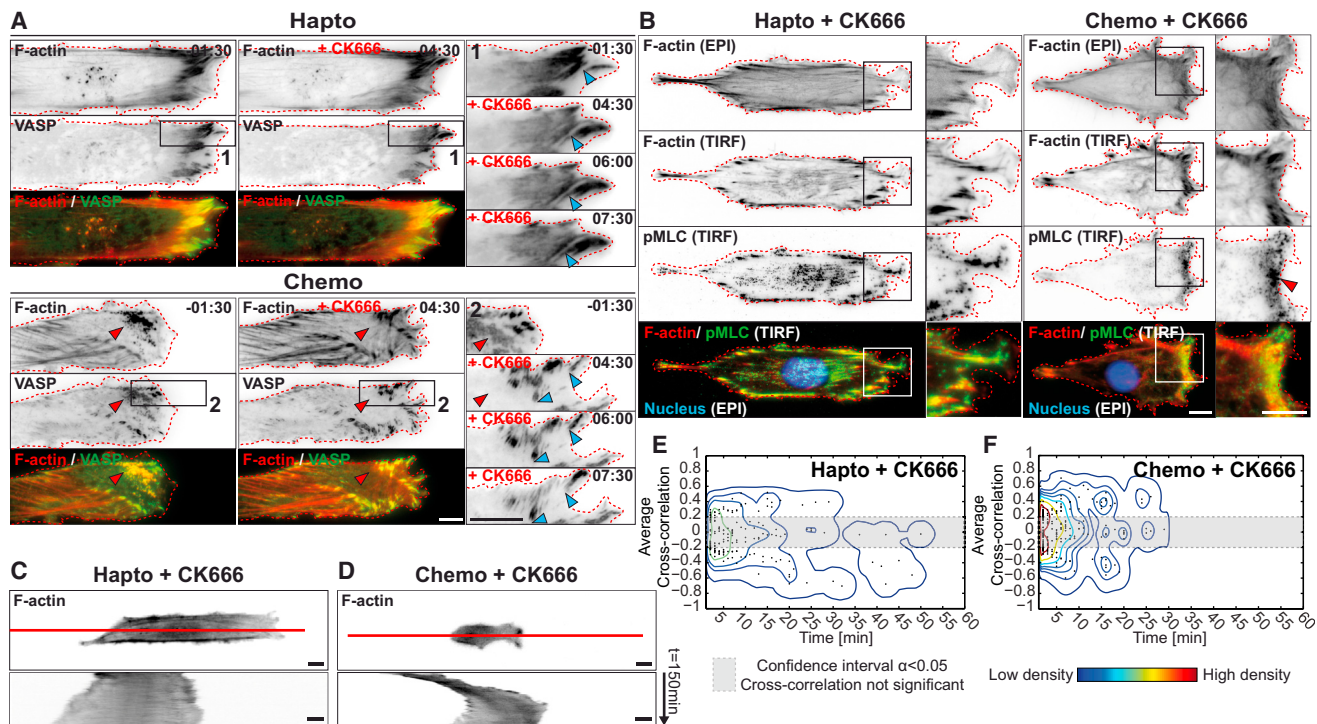
Micrographs and kymographs are shown in ibw contrast or as color composites.

(A) Representative high-resolution micrographs of F-actin and pMLC stainings. Hapto cells: red arrowhead indicates pMLC enrichment at the leading edge. Chemo cells: red arrowhead indicates pMLC in the myosin cluster behind the PLS zone.

(B) Representative micrographs of Lifeact-mCherry and MLC2a-GFP signals using TIRF. Dotted black/white lines delineate PLS and myosin zones.

(C) Kymograph analysis of F-actin and MLC2a dynamics along profiles shown in (B).

(legend continued on next page)

**Figure 7. Front PLS Module Perturbations**

Micrographs and kymographs are shown in bw contrast or as color composites.

(A) Representative TIRF micrographs (Lifeact-mCherry and VASP-GFP) and time-series (VASP-GFP) of haptic and chemo cells before and after PLSs disruption by Arp2/3 inhibition. Cells were incubated with 200 μ M CK666 at time 0:00. Red arrowheads indicate PLSs; blue arrowheads indicate focal adhesions.

(B) pMLC signals of haptic and chemo cells after 1 hr treatment with 200 μ M CK666. Red arrowhead indicates rescue of leading edge pMLC directly at the leading edge in chemo cells.

(C and D) Global morphodynamics of cells in response to acute Arp2/3 inhibition. Whole cell kymograph. Cells were imaged as in Figures 5D and 5E.

(E and F) 2D distribution of the average cross-correlation - duration of all instances of uniform qualitative behavior of haptic (E) and chemo (F) cells. $n = 12$ (haptic) and 8 (chemo) cells.

Scale bars represent 10 μ m (A–D).

zone prompted us to explore any potential role for RhoA signaling using RhoA2G, a FRET-based biosensor of RhoA activation (Fritz et al., 2013). In haptic cells, both on the line and plane substrates, RhoA was activated as a broad gradient spanning the entire lamella with activity decreasing from the leading edge to the cell center (Figures 8A and 8B, Haptic; Movie S8). This most likely results from an integrin-mediated mechano-sensing pathway impinging on RhoA (Guilluy et al., 2011). In chemo cells, low RhoA activity was observed at the PLS zone, but a highly focused region of lamellipodial RhoA activity remained (Figure 8A, Chemo; Movie S8). On the plane substrate, dynamic PLS motion correlated with local decrease of the lamellar RhoA activity, which immediately reappeared at sub-cellular regions in which PLSs vanish (Figure 8B, Chemo). This

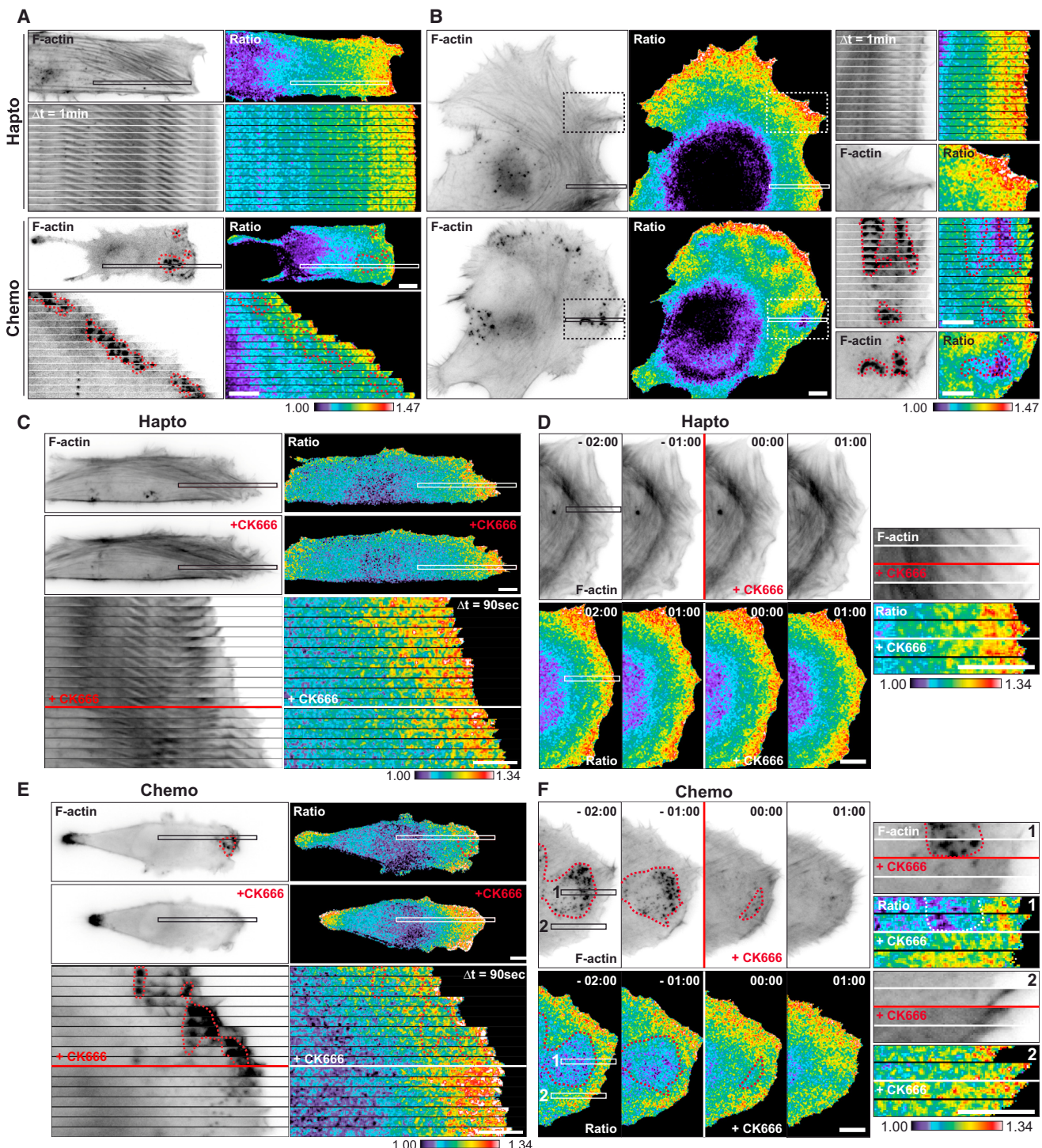
indicates an intimate spatio-temporal relationship between PLSs and low RhoA activity. We then acutely disrupted the PLS zone using CK666. In haptic cells, this did not affect the broad gradient of lamellar RhoA activity on both plane and line substrates (Figures 8C and 8D). In contrast, CK666-induced PLS disruption rescued the broad RhoA activation gradient at the front of chemo cells (Figure 8E). Identical results were observed on the plane substrate, again without any effect on RhoA activity in lamellar regions (Figure 8F). This indicates that the effects of CK666-mediated Arp2/3 inhibition on RhoA specifically correlate with PLS disruption, but do not affect lamellar RhoA signaling. Finally, identical results were obtained with the Src inhibitor PP2. PP2-induced PLS removal again led to immediate rescue of the broad RhoA activation pattern at the

(D and E) Global morphodynamics of haptic (D) and chemo (E) cells in response to acute myosin inhibition. Steady-state haptic or chemo cells expressing Lifeact-GFP were incubated with carrier or 10 μ M blebbistatin and immediately imaged using a 20 \times air objective. Single micrograph and whole cell kymographs are shown.

(F) 2D distribution of the average cross-correlation-duration of all instances of uniform qualitative behavior of haptic and chemo cells treated with 10 μ M blebbistatin. $n = 10$ (haptic) and 11 (chemo) cells.

(G and H) Instantaneous cell speed (G) and persistence (H) averaged between 6h and 12h after drug application. $n \geq 20$ cells per condition. *** $p < 0.0001$; Dunn's multiple comparison test. (G) Error bars represent SD. (H) Boxplots with median, interquartile (box), and data (whiskers) ranges are shown.

Scale bars represent 10 μ m (A–E).

**Figure 8. RhoA Activation Dynamics in Hapto and Chemo Cells**

Cells stably expressing the RhoA2G biosensor, and infected with an adenovirus encoding Lifeact-mCherry were imaged using EPI microscopy. RhoA activation, ratio images are color-coded according to scale bars. Lifeact-mCherry micrographs are shown in ibw contrast.

(A and B) Representative micrographs and kymographs of hapto and chemo cells on the line (A) and plane (B) substrates.

(C–F) Representative micrographs and kymographs of hapto (C and D) and chemo (E and F) cells before and after Arp2/3 inhibition on the line (C and E) and plane substrates (D and F). At the indicated time, cells were incubated with 200 μM CK666.

Scale bars represent 10 μm .

front of chemo cells, without however affecting lamellar RhoA activity in haptotactic cells (Figures S5E and S5F). These results indicate that the low contractility observed in the PLS zone correlates with decreased RhoA activity at this specific subcellular location.

DISCUSSION

PLSs Serve as a Spatially Organizing Module to Polarize Fibroblasts

Fibroblast migration has classically been studied on planar substrates with uniform coating that does not allow strong cell polarization. We show that PDGF stimulation of prepolarized fibroblasts leads to rapid and persistent migration in one direction for hours, in the absence of any gradient. Both initiation and maintenance of this polarized steady state correlates with the formation of a PLS zone, which allows to shape a subcellular region that exhibits low contractility (as characterized by loss of actin arcs and focal complex-focal adhesion maturation, and low myosin/RhoA activity). Such PLSs are not bona fide podosomes as described in macrophages (Calle et al., 2006) or in Src-transformed fibroblasts (Oikawa et al., 2008). However, similar structures have been observed before in NIH 3T3 fibroblasts (Collin et al., 2006).

Sustained persistent migration correlates with two emergent properties of the system. First, fibroblast prepolarization geometrically constrains the PLS zone proximal to the leading edge to hinder lamella formation, restricting contraction to the back of the cell. The establishment of a noncontractile, protrusive front and a contractile back allows for front/back uncoupling and efficient cell symmetry breaking. On the plane substrate, PLS zones with an identical function in the local decrease of lamellar contractility also exist. However, these only allow moderate polarization, most likely because they only disrupt the contractile lamellar networks observed throughout the cell periphery in local subsectors. Second, the dynamic properties of PLSs (Figures 3D and 3E) maintain the size and relative position of the PLS zone with time, indicating that PLSs function as a spatially organizing module that appropriately positions and coordinates front lamellipodium protrusion with back myosin retraction throughout the cell migration process. Future studies will be aimed at understanding the signaling and biophysical mechanisms that enable shaping of the mesoscale properties of the PLS zone. Similar spatially organizing cytoskeletal modules have already been proposed to regulate cytoskeletal polarity in neutrophils (Weiner et al., 2007). In the latter cells, the higher cytoskeletal plasticity and the intrinsically asymmetric cell shape might explain the absence of a requirement for prepolarization. It is also worth mentioning that persistent fibroblast migration has also been observed on 1 (but not 20) μm wide FN line substrate, which additionally mimic 3D ECM dimensionality (Doyle et al., 2009). However, this occurs in the absence of PLS structures, indicating that persistent migration can be mediated by multiple pathways. The requirement of a cytoskeletal, spatially organizing module for cell polarization has important consequences for experimental analysis of this system: signaling events that regulate cytoskeletal dynamics during persistent migration cannot be perturbed before acquisition of a polarized steady state, and thus, acute perturbations by pharmacological inhibition have to be used to study these pathways.

Functional Consequences of Front/Back Uncoupling

An important feature of persistent chemo cell migration is the uncoupling of front and back motions. The current model for front/back coordination of fibroblast migration posits that contraction of stress fibers connected to focal adhesions at the front generates forces on focal adhesions in the rear, promoting disassembly and tail retraction (Parsons et al., 2010). In prepolarized haptotactic cells, stress fiber arrays along the cell length indeed induce mechanical coupling between focal adhesions in the lamella and focal adhesions at the cell rear. However, this mechanical linkage admits only transient polarization episodes, and is insufficient to establish persistent migration. Although we cannot formally exclude that chemical signals lead to uncoupling of front/back motions in chemo cells, the finding that the PLS zone disrupts formation of a contractile lamella, restricts stress fibers and focal adhesions to the back and lateral parts of the cell, strongly suggests that the nature of the front/back uncoupling is mechanical by nature. Perturbation of the PLS zone using the CK666 compound leads to a rapid increase of myosin activity at the cell front, which is accompanied by focal adhesion maturation. This translates into front/back coupling and ultimately to loss of persistent migration. This strongly suggests the need for cell front and back uncoupling to maintain cell polarity and persistent migration.

One consequence of front/back uncoupling is the concentration of myosin activity behind the PLS zone promoting tail retraction. Surprisingly, stress fibers emanating from behind the PLS are not anchored to any adhesion structure within the myosin cluster. Most likely, the concentrated myosin zone is anchored at the back of the PLS zone through interaction with the lateral stress fiber-focal adhesion array. Importantly, chemo cells display lower levels of stress fibers and focal adhesions. Therefore, adhesion and contraction strength in these cells are adjusted so that lower rear contractility is still sufficient to promote rear focal adhesions disassembly. Similar myosin clusters have been observed at the back but not at the front of neutrophils (Pestonjamasp et al., 2006) and fish keratocytes (Svitkina et al., 1997), which both migrate rapidly and highly persistently. Hence, we speculate that a rear-concentrated myosin module may be a general feature of rapid, persistent migration.

An additional consequence of front/back uncoupling is the appearance of a potent increase in protrusion velocity and persistence at the front. This seems to enable highly processive leading edge advancement that might explain the rapid migration speed of chemo cells. Here, the absence of a contractile lamella might optimize the functional output of the lamellipodial actin treadmill at the leading edge. Our data imply that the Arp2/3 complex is involved but not required for this membrane protrusion mode. Together, these observations suggest that front/back uncoupling leads to fast cell migration by promoting efficient lamellipodial protrusion without inhibitory lamellar contraction at the front and by forming a loosely anchored myosin module that is just strong enough to dissolve rear focal adhesions.

Spatiotemporal Control of RhoA Activity at the PLS Zone

Our FRET imaging studies suggest that a broad gradient of RhoA in haptotactic cells from the leading edge regulates lamellar myosin contractility, most likely through Rho kinase-mediated control of MLC (Burridge and Wennerberg, 2004). In chemo cells, the

PLS zone dynamically correlates with reduced RhoA activity. Acute removal of the PLS zone using two pharmacological compounds that operate through distinct modes of action, and do not affect lamellar RhoA activity, restores the broad RhoA activity gradient, pMLC signal, and contractile structures. This indicates a local, negative reciprocal crosstalk between PLSs and RhoA within the PLS zone. By locally lowering contractility, PLSs might switch off a positive feedback in which RhoA-specific GEFs such as LARG or GEF-H1 (Guilluy et al., 2011) translate mechanical activation of integrins by contractile forces into RhoA activation upstream of myosin II. An interesting result is that, in absence of a lamella, chemo cells still display a highly focused zone of active RhoA directly in the lamellipodium not visible in haptocells. Our previous work has already established that two pools of RhoA activity can exist at the leading edge: a broad gradient and a focused band directly at the edge that correlates specifically with the onset of robust membrane protrusion (Machacek et al., 2009; Pertz et al., 2006). We propose that in chemo cells the former is switched off in conjunction with the inhibition of the lamella by the PLS, leaving the edge-focused RhoA activity pool to regulate membrane protrusion, e.g., through the effectors mDia1/2 (Palazzo et al., 2001). As previously documented (Pertz et al., 2006), additional RhoA activation pools can be observed in retracting tails (Figures 8C and 8E), but not at the myosin cluster observed behind the PLS zone in chemo cells. These results reveal a complex spatiotemporal RhoA activation landscape that correlates with the induction of specific cytoskeletal structures. This also suggests the existence of multiple signaling pathways that regulate different subcellular myosin pools.

Significance of Chemokinesis in Directional Cell Migration

Our results show that growth factor-induced, persistent fibroblast migration does not necessarily require a chemotactic gradient. Chemokinesis is sufficient to lock the cell in a polarized state of persistent migration. This has important consequences for the regulation of directed cell migration *in vivo*. During development, this might be useful during collective, directional migration of neural crest cells, in which chemokinesis and contact inhibition cooperate to generate an overall polarity to the cell population (Theveneau and Mayor, 2012). During cancer metastasis, a macrophage-tumor cell paracrine loop that involves secretion of growth factors from the two different cell types allows for collective cell streaming in one specific direction on collagen fibrils (Roussos et al., 2011). Although this was proposed to involve chemotaxis, it is conceivable that chemokinesis might be sufficient to induce directional cell movement on the highly asymmetric collagen fiber. In both cases, the ability of a chemokinetic stimulus to hardwire directionality of prepolarized cells might therefore provide a means for generation of persistent, directional cell migration.

EXPERIMENTAL PROCEDURES

Line Substrate Microfabrication

Polydimethylsiloxane (PDMS) ridge stamps were used as a template to produce the line substrate (20 μm wide ridge structures separated by 100 μm wide gaps) on glass coverslips (Figure S1D). PDMS was mixed well in a ratio of 10:1 with curing agent (Sylgard 184 Silicone Elastomeric KIT; Dow Corning) and poured onto a silicon wafer produced by soft lithography. Vacuum was

applied to remove enclosed air bubbles and PDMS was cured by incubation for 2 hr at 70°C. The polymer was then peeled off the silicon wafer and cut into pieces with adequate dimensions. PDMS-based live cell chambers consisting of a square chamber (5 mm width, 6 mm length, 100 μm high roof) connected to an inlet and an outlet were constructed the same way using specific silicon wafers.

Glass coverslips (24 \times 50 mm) were extensively cleaned with anhydrous ethanol and demineralized water and were coated with 0.5 mg/ml poly-Lysine-polyethylene glycol, (PLL-PEG; SUSOS) for 30 min at room temperature. Next, the glass coverslip was once washed with water and dried. In the meanwhile, the PDMS ridge stamp and PDMS live cell chamber were cleaned with tape at the structured surface. The PDMS ridge stamp was then aligned on the PLL-PEG coated surface of the glass coverslip and exposed to plasma etching at 100% power for 90 s using a CUTE plasma oven (Femto Science). The glass coverslips (with PDMS ridge stamp) as well as the PDMS-based live cell imaging chamber (structured side up) were treated with plasma for an additional 30 s. The PDMS ridge stamp was then removed and the PDMS-based live cell-imaging chamber was grafted on the glass coverslip on top of the line substrate. Once the PDMS-based live cell-imaging chamber was covalently bound to the glass coverslip, fibronectin was coated overnight at 4°C at 10 $\mu\text{g}/\text{ml}$. Line substrates were then washed once with PBS and once with imaging medium. Five microliters of a suspension containing 2×10^5 cells/ml was loaded into the microfluidic device. Loading cells in such a small volume minimized flow and improved cell attachment. After 30 min, when cells had adhered, the inlet and outlet of the microfluidic device were filled with imaging medium and the devices were kept in an incubator until live cell imaging.

Image Analysis

Basic image analysis and processing was performed using MetaMorph software. FRET data were analyzed as described elsewhere (Fritz et al., 2013). Cell edge dynamics as shown in Figure 4 were quantified using in-house MATLAB-based software (MathWorks). This software calculates the velocities by tracking the displacement of all pixels at the cell edge from one frame to the next (Machacek and Danuser, 2006). The pixel-wise velocities were averaged within sampling windows of approximately 1 μm width placed along the cell edge. This averaging step gave rise to the final velocities used for analysis. We further analyzed the edge dynamics by clustering regions of the cell edge with similar velocity magnitude. A fuzzy k-means algorithm was used for this purpose (Nock and Nielsen, 2006).

Analysis of Global Fibroblast Morphodynamics

To analyze global properties of fibroblasts migrating on the line substrate, a computer vision algorithm was developed to measure the kinematic parameters from different cell regions. These analyses were all performed on time-lapse movies of fibroblasts stably expressing Lifeact-GFP, which provide adequate contrast for the segmentation of the cell boundary using intensity-based thresholding. The basic idea behind this algorithm is to separately capture the motion from the left, central, and right regions of the cell by reducing these areas to single points. After segmentation, the algorithm calculates the cell centroid. The centroid point is then used to divide the cell in half where the dividing plane is perpendicular to the long axis of the migration path. Once divided, each cell half is reflected over the same dividing plane to form a closed symmetric object. An ellipse is then inscribed to both objects and the foci coordinates are calculated (Figure 1E). The right and left ellipse foci from the right and left mirrored halves, respectively, were used to quantify the motion for the right and left regions. The motion of the center region was quantified by the centroid. Two important aspects are achieved with this approach: independence between right/left measurements and the ability to include local cell morphology from the right/left regions to capture their respective motions. In addition to the velocities described above, the algorithm also calculates the cell length (Figure 1H).

Cell Velocity Analysis

Visual inspection of haptocells and chemo cells revealed a clear difference of cell displacement over time. To quantify the different migration modes, we implemented an algorithm based on a time series analysis technique called empirical mode decomposition (Wu et al., 2007). This algorithm locally decomposes the centroid instantaneous velocity into two frequency components: a fast component (including quick changes in velocity direction) and a slow

component (including the overall trend in velocity). The fast component was used to estimate an interval that represents the distribution of magnitudes for the fast, quasirandom changes in velocity. The interval was locally estimated using a sliding window of 10 points with reflective boundaries in order to accommodate temporal variations of the fast component. The range values were calculated from the spread of the fast component within the 10 points window (± 3 SD centered in 0).

We defined as bidirectional migration, periods in which the slow component of the centroid velocity was contained in the fast component interval. That means the cell changes direction from one frame to the next, having little or no displacement. Unidirectional migration mode was defined as periods in which the slow component is outside the fast component interval. Although there is a possibility of change in direction, this scenario indicates that the cell has an overall displacement in one direction. We used left-to-right as the direction of positive migration. The front region of the cell was defined as the side corresponding to the direction of centroid motion and left/right foci velocities were labeled as front/back accordingly (Figure 1G).

Front/Back Coordination Quantification

We used time-dependent cross-correlation to test the coordination between the front and back regions of the cell. Given two time series $x(t)$ and $y(t)$, the time-dependent cross-correlation is defined as:

$$\rho(t) = \frac{1}{W+1} \sum_{i=t-W/2}^{t+W/2} \frac{(y_i - \bar{y})(x_i - \bar{x})}{\sigma_y \sigma_x},$$

where $W+1$ is the length of the sliding window and $\sigma_x, \sigma_y, \bar{x}, \bar{y}$ denote the SDs and means for x and y within the sliding window. The coupling between front and back regions was estimated by replacing x and y with front/back instantaneous velocities. Positive values indicate front and back moving in the same direction. The confidence interval around zero correlation was estimated based on asymptotic distribution analysis for the cross-correlation of two random Gaussian processes (Box et al., 1994). Correlations values inside this interval are statistically insignificant.

Average Cross-Correlation Distributions

The time-dependent cross-correlation plots showed a transient nature of the front/back coordination with periods of negative, insignificant, and positive cross-correlation. To better summarize this variability in behavior for the entire data set, we plotted the 2D distribution of the interval length and its respective average cross-correlation for three qualitative behaviors (Figure S1).

Additional details can be found in the [Supplemental Experimental Procedures](#).

SUPPLEMENTAL INFORMATION

Supplemental Information includes Supplemental Experimental Procedures, five figures and eight movies and can be found with this article online at <http://dx.doi.org/10.1016/j.devcel.2014.07.022>.

ACKNOWLEDGMENTS

We are grateful to Johan De Rooij, Alan Howe, Matthias Kaeser, Olivier Destaing, and Ana-Maria Lennon-Duménil for sharing reagents and to Eugene Tkachenko and Bernhard Wehrle-Haller for comments on the manuscript. This work was supported by grants from the Swiss National Science Foundation to O.P., and from the Human Frontier Science Program to O.P., G.D., and N.L.J. M.V. was supported by an Institutional Training Grant NIH/NRSA 1F32GM103278-01.

Received: October 22, 2013

Revised: April 17, 2014

Accepted: July 28, 2014

Published: September 29, 2014

REFERENCES

- Albiges-Rizo, C., Destaing, O., Fourcade, B., Planus, E., and Block, M.R. (2009). Actin machinery and mechanosensitivity in invadopodia, podosomes and focal adhesions. *J. Cell Sci.* 122, 3037–3049.
- Box, G.E.P., Jenkins, G.M., and Reinsel, G.C. (1994). *Time Series Analysis: Forecasting and Control*, Third Edition. (Englewood Cliffs: Prentice Hall).
- Burridge, K., and Wennerberg, K. (2004). Rho and Rac take center stage. *Cell* 116, 167–179.
- Calle, Y., Burns, S., Thrasher, A.J., and Jones, G.E. (2006). The leukocyte podosome. *Eur. J. Cell Biol.* 85, 151–157.
- Collin, O., Tracqui, P., Stephanou, A., Usson, Y., Clément-Lacroix, J., and Planus, E. (2006). Spatiotemporal dynamics of actin-rich adhesion micro-domains: influence of substrate flexibility. *J. Cell Sci.* 119, 1914–1925.
- Doyle, A.D., Wang, F.W., Matsumoto, K., and Yamada, K.M. (2009). One-dimensional topography underlies three-dimensional fibrillar cell migration. *J. Cell Biol.* 184, 481–490.
- Friedl, P., and Wolf, K. (2010). Plasticity of cell migration: a multiscale tuning model. *J. Cell Biol.* 188, 11–19.
- Fritz, R.D., Letzelter, M., Reimann, A., Martin, K., Fusco, L., Ritsma, L., Ponsioen, B., Fluri, E., Schulte-Merker, S., van Rheezen, J., and Pertz, O. (2013). A versatile toolkit to produce sensitive FRET biosensors to visualize signaling in time and space. *Sci. Signal.* 6, rs12.
- Guilluy, C., Swaminathan, V., Garcia-Mata, R., O'Brien, E.T., Superfine, R., and Burridge, K. (2011). The Rho GEFs LARG and GEF-H1 regulate the mechanical response to force on integrins. *Nat. Cell Biol.* 13, 722–727.
- Hotulainen, P., and Lappalainen, P. (2006). Stress fibers are generated by two distinct actin assembly mechanisms in motile cells. *J. Cell Biol.* 173, 383–394.
- Kim, D.H., Provenzano, P.P., Smith, C.L., and Levchenko, A. (2012). Matrix nanotopography as a regulator of cell function. *J. Cell Biol.* 197, 351–360.
- Machacek, M., and Danuser, G. (2006). Morphodynamic profiling of protrusion phenotypes. *Biophys. J.* 90, 1439–1452.
- Machacek, M., Hodgson, L., Welch, C., Elliott, H., Pertz, O., Nalbant, P., Abell, A., Johnson, G.L., Hahn, K.M., and Danuser, G. (2009). Coordination of Rho GTPase activities during cell protrusion. *Nature* 461, 99–103.
- Murphy, D.A., and Courtneidge, S.A. (2011). The ‘ins’ and ‘outs’ of podosomes and invadopodia: characteristics, formation and function. *Nat. Rev. Mol. Cell Biol.* 12, 413–426.
- Nock, R., and Nielsen, F. (2006). On weighting clustering. *IEEE Trans. Pattern Anal. Mach. Intell.* 28, 1223–1235.
- Nolen, B.J., Tomasevic, N., Russell, A., Pierce, D.W., Jia, Z., McCormick, C.D., Hartman, J., Sakowicz, R., and Pollard, T.D. (2009). Characterization of two classes of small molecule inhibitors of Arp2/3 complex. *Nature* 460, 1031–1034.
- Oikawa, T., Itoh, T., and Takenawa, T. (2008). Sequential signals toward podosome formation in NIH-src cells. *J. Cell Biol.* 182, 157–169.
- Palazzo, A.F., Cook, T.A., Alberts, A.S., and Gundersen, G.G. (2001). mDia mediates Rho-regulated formation and orientation of stable microtubules. *Nat. Cell Biol.* 3, 723–729.
- Parsons, J.T., Horwitz, A.R., and Schwartz, M.A. (2010). Cell adhesion: integrating cytoskeletal dynamics and cellular tension. *Nat. Rev. Mol. Cell Biol.* 11, 633–643.
- Pertz, O., Hodgson, L., Klemke, R.L., and Hahn, K.M. (2006). Spatiotemporal dynamics of RhoA activity in migrating cells. *Nature* 440, 1069–1072.
- Pestonjamasp, K.N., Forster, C., Sun, C., Gardiner, E.M., Bohl, B., Weiner, O., Bokoch, G.M., and Glogauer, M. (2006). Rac1 links leading edge and uropod events through Rho and myosin activation during chemotaxis. *Blood* 108, 2814–2820.
- Petrie, R.J., Doyle, A.D., and Yamada, K.M. (2009). Random versus directionally persistent cell migration. *Nat. Rev. Mol. Cell Biol.* 10, 538–549.
- Pollard, T.D., and Borisy, G.G. (2003). Cellular motility driven by assembly and disassembly of actin filaments. *Cell* 112, 453–465.
- Ponti, A., Machacek, M., Gupton, S.L., Waterman-Storer, C.M., and Danuser, G. (2004). Two distinct actin networks drive the protrusion of migrating cells. *Science* 305, 1782–1786.
- Riedl, J., Crevenna, A.H., Kessenbrock, K., Yu, J.H., Neukirchen, D., Bista, M., Bradke, F., Jenne, D., Holak, T.A., Werb, Z., et al. (2008). Lifeact: a versatile marker to visualize F-actin. *Nat. Methods* 5, 605–607.

- Roussos, E.T., Condeelis, J.S., and Patsialou, A. (2011). Chemotaxis in cancer. *Nat. Rev. Cancer* **11**, 573–587.
- Straight, A.F., Cheung, A., Limouze, J., Chen, I., Westwood, N.J., Sellers, J.R., and Mitchison, T.J. (2003). Dissecting temporal and spatial control of cytokinesis with a myosin II Inhibitor. *Science* **299**, 1743–1747.
- Svitkina, T.M., Verkhovsky, A.B., McQuade, K.M., and Borisy, G.G. (1997). Analysis of the actin-myosin II system in fish epidermal keratocytes: mechanism of cell body translocation. *J. Cell Biol.* **139**, 397–415.
- Theveneau, E., and Mayor, R. (2012). Neural crest delamination and migration: from epithelium-to-mesenchyme transition to collective cell migration. *Dev. Biol.* **366**, 34–54.
- Weiner, O.D., Marganski, W.A., Wu, L.F., Altschuler, S.J., and Kirschner, M.W. (2007). An actin-based wave generator organizes cell motility. *PLoS Biol.* **5**, e221.
- Wu, Z., Huang, N.E., Long, S.R., and Peng, C.K. (2007). On the trend, detrending, and variability of nonlinear and nonstationary time series. *Proc. Natl. Acad. Sci. USA* **104**, 14889–14894.
- Wu, C., Asokan, S.B., Berginski, M.E., Haynes, E.M., Sharpless, N.E., Griffith, J.D., Gomez, S.M., and Bear, J.E. (2012). Arp2/3 is critical for lamellipodia and response to extracellular matrix cues but is dispensable for chemotaxis. *Cell* **148**, 973–987.
- Zamir, E., Katz, B.Z., Aota, S., Yamada, K.M., Geiger, B., and Kam, Z. (1999). Molecular diversity of cell-matrix adhesions. *J. Cell Sci.* **112**, 1655–1669.